Condensed Matter Physics, 2021, Vol. 24, No. 2, 23705: 1–11
DOI: 10.5488/CMP.24.23705
http://www.icmp.lviv.ua/journal

CONDENSED MATTER PHYSICS

Mn ions' site and valence in $PbTiO_3$ based on the native vacancy defects

H. Xin, *Q. Pang, D. L. Gao, L. Li, P. Zhang, J. Zhao

College of Science, Xi'an University of Architecture and Technology, Xi'an 710055, China

Received January 28, 2021, in final form April 15, 2021

Mn ions' doping site and valence were studied in $PbTiO_3$ (PT) with the native vacancy defects by the first-principles calculations. Firstly, the native vacancy defects of Pb, O and Ti in PT were investigated and it was found that Pb vacancy is preferred to others. And then the growth of Mn doped PT should be preferred to Mn ion substituting for an A-site Pb ion with +3 valence when Pb is deficient under equilibrium conditions driven solely by minimization of the formation energy, and this could result in a larger lattice distortion of PT. In addition, when Mn enters the Pb site, the electronegativity of O becomes weaker which makes the domain movement easier in PT to improve the performance of PT, while Mn ion substitution for a B-site Ti ion is the opposite.

Key words: *Mn doping, PT, native defects, defect formation energy, Bader charge*

1. Introduction

The advantage of lead titanate $PbTiO_3$ (PT) and lead zirconate titanate $PbZr_{1-x}Ti_xO_3$ (PZT) as Pb-based ferroelectric materials, has been well exhibited in infrared pyroelectric sensors, piezoelectric transducers, nonvolatile memories and so on [1–4]. Furthermore, some cations were also introduced to modify their properties and improve their applications [5–15]. Mn doped PT and PZT exhibiting different characteristics with dopant concentration have attracted a lot of interest [14–18]. Especially, Mn can have a softening effect on PT and PZT at a small concentration [14, 16, 17]. It was deemed that the occurrence of a small amount of Mn ions entering the A site was compatible with small differences between the calculated and measured x-ray absorption near-edge structures (XANES) [19]. Then, it acts as a B-site dopant to decrease the relative permittivity and loss tangent with the concentration increasing. The effect of Mn doping on the structure of PT and PZT is still not well understood.

Mn defects could always occur with native defects simultaneously during the formation process of Mn doped PT and PZT. Several native defects have been reported, such as Pb vacancy (V_{Pb}) [20], O vacancy (V_O) [20] and Ti vacancy (V_{Ti}) [21], which may affect the role of Mn in PT and PZT. Thus, the study of Mn doped PT and PZT should be carried out based on the native defects. In this paper Mn defect in PT is studied by the first-principles calculation due to their similar structure, which would be helpful to clarify the influence of Mn doping on PZT.

In this paper, the native vacancy defects of PT were investigated by the first-principles calculation firstly. Their stability was analyzed through the defect formation energy which is a function of Fermi-energy under different growth conditions. Then, Mn defect position and valence state in PT were determined based on the most probable native vacancy defects. Additionally, the electronegativity of O was investigated in PT without and with Mn doping at different sites, and its effect on the performance of PT was discussed too.

*Email address: xinhong@xauat.edu.cn.

2. Model structures and computational methods

2.1. Model structures

The cubic phase of PT (space group Pm3m), which is often used in the first principles simulations, was chosen as a model to simplify the calculation [22]. For simulations, a $3 \times 3 \times 3$ supercell [shown in figure 1 (a)] composed of 135 atoms and 27 primitive PT unit cells was established by repeating the unit cell. Then, one vacancy defect (such as V_{Pb}, V_O and V_{Ti}) was introduced into the $3 \times 3 \times 3$ supercell for the calculation of the native vacancy defect. It is difficult to show the structure of defects in PT with the dense ion arrangement. Thus, $2 \times 2 \times 2$ supercells were used to illustrate the structure of defects in PT in figures 1 (b) to (h). Additionally, the model structures of Mn defects in PT were built by adding one Mn ion into two kinds of host supercells, one $3 \times 3 \times 3$ perfect supercell of PT [marked with model #1 in figures 1 (e) and 1 (f)] and the other containing one vacancy defect [marked with model #2 in figures 1 (g) and 1 (h) where V_{Pb} was taken as an example]. The concentrations of native defects and Mn defects are all 3.7% in the calculation, while it is about 3% for Mn doping in the experiment [16].

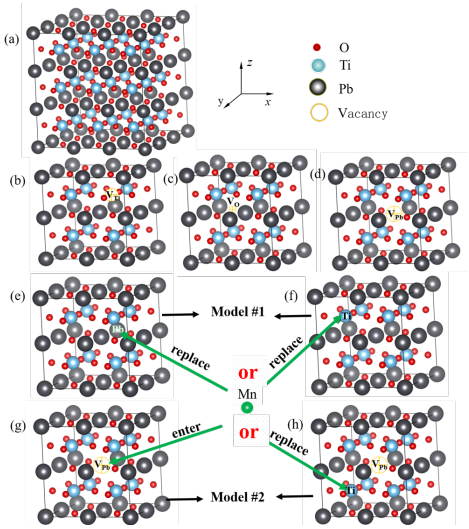

Figure 1. (Colour online) The model structures PT without and with different defects, (a) $3 \times 3 \times 3$ perfect supercell, (b) to (h) $2 \times 2 \times 2$ supercells for different defects, (b) V_{Ti}, (c) V_O, (d) V_{Pb}, and (e) to (h) schematics showing Mn doping into Pb site and Ti site in two kinds of host supercells, respectively, (e) and (f) perfect supercells marked with model #1, (g) and (h) supercells with one V_{Pb} marked with model #2. Red balls, blue balls, grey balls, hollow yellow balls and a green ball denote O, Ti, Pb ions, Pb vacancy (V_{Pb}) and a Mn ion, respectively.

2.2. Computational methods

2.2.1. First-principles

All the total energy calculations were performed in VASP code using the projector-augmented wave (PAW) method [23, 24]. Generalized gradient approximations (GGA) were used in the form of Perdew-Burke-Ernzerhof (PBE) exchange-correlation function for the electron-electron interaction [25]. A Monkhorst-Pack mesh and a plane-wave cutoff energy were determined at $6 \times 6 \times 6$ and 500 eV, respectively, through calculating the total energy. The convergence of the electronic self-consistent energy less than 10^{-5} eV and the force on each atom less than 0.01 eV/Å were defined for full relaxation of the positions of all atoms.

The optimized lattice constant of PT is 3.972 Å, which is very close to the experimental value of 3.97 Å [22]. The band gap of PT was calculated to be 2.40 eV in this paper, which is lower than the

experimental value of 3.40 eV [26]. The band gap is always undervalued with the first-principles [27, 28], so the experimental value of 3.40 eV was used in calculation presented below.

2.2.2. Defect formation energies

The defect formation energy $E_f(D^q)$ of a defect D in the charge state q is defined as [29, 30]:

$$E_f(D^q) = E_{\text{tot}}(D^q) - E_{\text{tot}} \pm \sum_i n_i \mu_i + q(\varepsilon_{\text{F}} + E_V + \Delta V), \tag{2.1}$$

where $E_{\text{tot}}(D^q)$ and E_{tot} are the total energy of the supercell with and without defect, respectively, n_i is the number of i atoms which are removed from (or added to) the supercell corresponding to plus (or minus) sign, μ_i is its chemical potential, q is the charge state of the defect, ε_{F} is Fermi-energy which is calibrated to 0 at the top of the valence band E_V. Finally, a correction term ΔV is added to align the reference potential in the defect supercell with that in the bulk.

When the defect formation energies $E_f(D^{q_1})$ and $E_f(D^{q_2})$ in two charge states of q_1 and q_2 are equal, the defect transition Fermi-energy $\varepsilon_{q_1-q_2}$, which is defined as the thermodynamic transition level [29], can be determined as the following form according to equation (2.1):

$$\varepsilon_{q_1-q_2} = \frac{E_{\text{tot}}(D^{q_1}) - E_{\text{tot}}(D^{q_2})}{q_2 - q_1} - E_V - \Delta V. \tag{2.2}$$

To grow the crystal of $PbTiO_3$ in thermodynamic equilibrium conditions, μ_{Pb}, μ_{Ti}, μ_{O} and μ_{PbTiO_3} (the chemical potentials of Pb, Ti, O and $PbTiO_3$) must be satisfied as follows:

$$\mu_{\text{Pb}} + \mu_{\text{Ti}} + 3\mu_{\text{O}} = \mu_{PbTiO_3}. \tag{2.3}$$

PbO_2, PbO and TiO_2 are considered to be major competing phases. The following conditions need to be further taken into account in order to inhibit the undesired phases in $PbTiO_3$ [31]

$$\begin{aligned} &\mu_{\text{Pb}} \leqslant 0, \quad \mu_{\text{Ti}} \leqslant 0, \quad \mu_{\text{O}} \leqslant 0, \\ &\mu_{\text{Pb}} + 2\mu_{\text{O}} < \mu_{PbO_2}, \\ &\mu_{\text{Pb}} + \mu_{\text{O}} < \mu_{\text{PbO}}, \\ &\mu_{\text{Ti}} + 2\mu_{\text{O}} < \mu_{TiO_2}, \\ &\mu_{\text{Pb}} + \mu_{\text{Ti}} \geqslant \mu_{PbTiO_3}, \end{aligned} \tag{2.4}$$

where μ_{PbO_2}, μ_{PbO} and μ_{TiO_2} are the chemical potentials of corresponding competing phases. Their corresponding bulk energies of per formula unit are listed in table 1.

The chemical potentials of Pb, Ti and O, μ_{Pb}, μ_{Ti} and μ_{O}, could be determined from equations (2.3) and (2.4) for stable $PbTiO_3$ growth, which were shown on the μ_{Pb}-μ_{Ti} plane in figure 2 with a shaded region. Then, the chemical potentials at four vertices (labeled with A, B, C, and D in figure 2, respectively) of the quadrilateral shadow region, listed in table 2, were selected to analyze the defect formation energies, which correspond to four different growth conditions of stable PT growth. A and B points represent the

Table 1. Bulk energies of per formula unit of competing phases of PT.

System	E_{bulk} (eV)
$PbTiO_3$	−13.00
TiO_2	−9.95
PbO	−2.85
PbO_2	−3.66

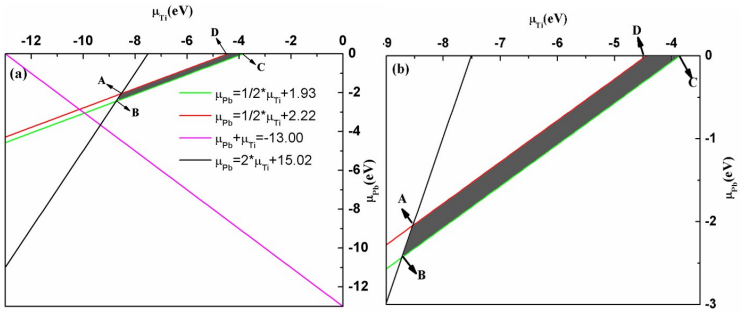

Figure 2. (Colour online) Region of stability (shaded) for $PbTiO_3$ in the 2D space spanned by μ_{Ti} and μ_{Pb}, (a) full scale and (b) the magnified stable region. The (colored) lines are the limits from the compound of interest and the competing phases. A, B, C, and D are four vertices of that region corresponding to four different growth conditions of stable PT growth.

Table 2. Chemical potentials of Ti, Pb and O (μ_{Ti}, μ_{Pb} and μ_O) at A, B, C and D four vertices of the shadow region in figure 2.

Chemical potential	μ_{Ti} (eV)	μ_{Pb} (eV)	μ_O (eV)
A	−8.56	−2.05	−0.80
B	−8.73	−2.43	−0.61
C	−3.86	0	−3.047
D	−4.44	0	−2.85

oxygen-rich growth of PT, where μ_O is higher, while C and D points are oxygen-poor, which correspond to μ_O in table 2. However, they are just opposite for Ti and Pb. Since the amount of Mn doping was very small, the change of chemical potential of Mn was neglected and the energy −5.16 eV of Mn atom in their bulk crystal phase was used in the calculation. For simplicity, Mn_{Pb}^{x+} and Mn_{Ti}^{x+} were used to represent the defects of Mn ions in $+x$ valence state entering the Pb site and Ti site, respectively, in this paper.

3. Results and discussion

3.1. Analysis of native vacancy defects

The dependence of the formation energies on ε_F for native vacancy defects was shown in figure 3 in four different growth conditions which were illustrated with A, B, C and D in figure 2. These results were obtained from the first-principles calculations according to equation (2.1) and the slope of the line represents the charge state of the native vacancy defect. There is a little difference between figures 3 (a) to (d) which can be attributed to the chemical potentials of Pb, Ti and O in four growth conditions. It could be seen that the vacancy formation energy for Pb is generally lower than those for others at all growth conditions as shown in figure 3. It could be concluded that V_{Pb}'s, usually caused by Pb volatilization, are most likely to be formed during the growth process of PT. Our results are consistent with the conclusion drawn in the experiment [20].

3.2. Analysis of Mn defects

3.2.1. Energies

Since V_{Pb} is the most probable vacancy defect during the growth process of PT, usually it is possible that a few V_{Pb}'s still exist in PT though the excess Pb is added during preparation process of PT. Thus, Mn defects in PT should be studied based on the Pb vacancy defects. In order to study the effect of V_{Pb} on Mn doping in the PT crystal, one Mn impurity is added into Pb site and Ti site in the two kinds of

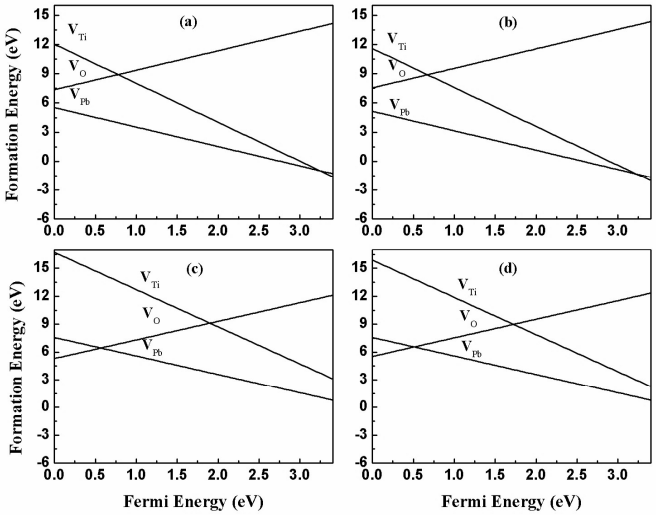

Figure 3. Formation energies as a function of Fermi level for vacancy defects in PT in four different growth conditions which were illustrated with A, B, C and D in figure 2. The zero of Fermi level corresponds to the top of the valence band. The slope of these lines indicates the charge state. (a), (b), (c) and (d) correspond to A, B, C and D, four different growth conditions, respectively.

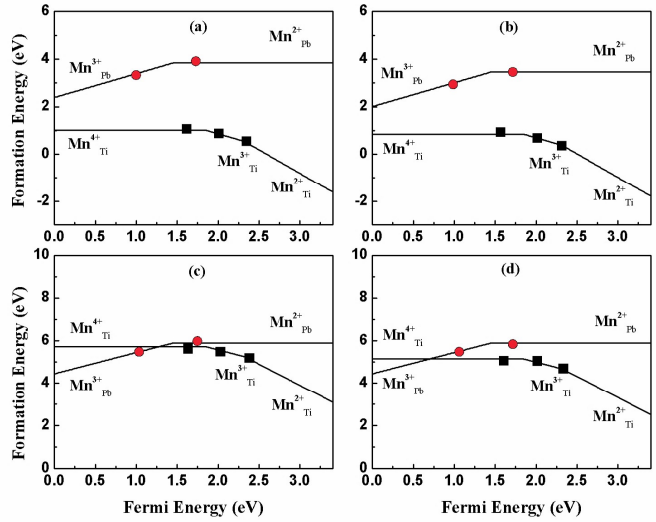

Figure 4. (Colour online) Formation energies as a function of Fermi level for Mn in different configurations (Pb-substitutional, Ti-substitutional) in the host supercell without V_{Pb} in different growth conditions. Kinks in the curves indicate transitions between different charge states. Red solid circles and black solid squares represent the defect formation energies of Mn_{Pb} and Mn_{Ti} at corresponding Fermi levels in different charge states respectively. (a), (b), (c) and (d) correspond to A, B, C and D, four different growth conditions in figure 2, respectively.

$3 \times 3 \times 3$ host supercells, respectively. The perfect supercells were marked with model #1 and those with one V_{Pb} were marked with model #2 as shown in figures 1 (e) to (h).

In model #1, V_{Pb} is not considered in Mn doped PT. The formation energies of Mn defects in different valence states and sites were investigated and discussed in this case firstly. Figure 4 shows the formation energy as a function of ε_F for Mn in different configurations with four different growth conditions. The

Table 3. Transition levels $\varepsilon_{q_1-q_2}$ (eV) of different charge states for Mn defects which are the kinks on the curves in figure 4 (Mn doped PT without V_{Pb}) and figure 5 (Mn doped PT with V_{Pb}).

	Mn doped PT without V_{Pb}			Mn doped PT with V_{Pb}		
	$Mn_{Pb}^{3+} \rightarrow Mn_{Pb}^{2+}$	$Mn_{Ti}^{4+} \rightarrow Mn_{Ti}^{3+}$	$Mn_{Ti}^{3+} \rightarrow Mn_{Ti}^{2+}$	$Mn_{Pb}^{3+} \rightarrow Mn_{Pb}^{2+}$	$Mn_{Ti}^{4+} \rightarrow Mn_{Ti}^{3+}$	$Mn_{Ti}^{3+} \rightarrow Mn_{Ti}^{2+}$
$\varepsilon_{q_1-q_2}$	1.46	1.85	2.32	1.46	0.98	1.05

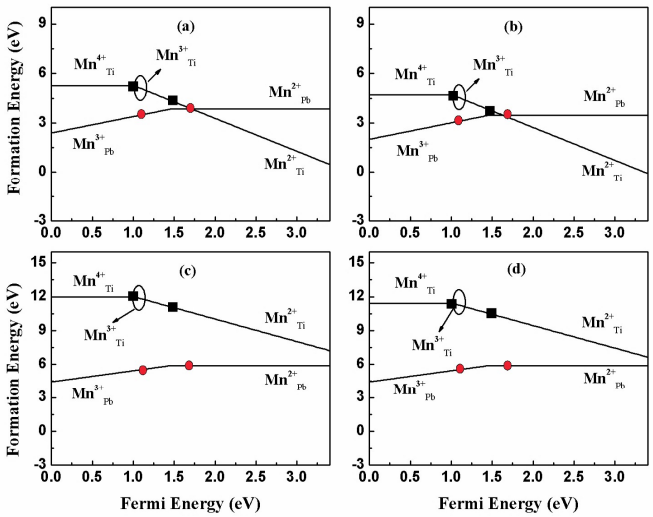

Figure 5. (Colour online) Formation energies vs Fermi energy for the defects of Mn_{Pb} and Mn_{Ti} at each relevant charge state in the host supercell with V_{Pb} in different growth conditions. Red solid circles and black solid squares have the same meaning as in figure 4. (a), (b), (c) and (d) correspond to A, B, C and D, four different growth conditions in figure 2, respectively.

line segments of a different slope were displayed corresponding to different charge states and they connect each other at the corresponding transition level for the same doping defect. The corresponding transition levels are listed in table 3. The formation energies increase with ε_F and decreasing of Mn ion's valence for Mn_{Pb}, while those are contrary for Mn_{Ti}. Furthermore, the neutral charge states have obviously higher energies than other charge states for both Mn_{Pb} and Mn_{Ti}. It indicated that Mn ion doping into Pb site at a higher valence is more stable, while it is more stable for Mn_{Ti} at a lower valence, only considering the defect formation energies. It is also noted that the formation energies of Mn_{Ti} are always much lower than those of Mn_{Pb} in figures 4 (a) and 4 (b) corresponding to the oxygen-rich growth, while they increase and get close to each other in figures 4 (c) and 4 (d) corresponding to the oxygen-poor growth, which results from the varieties of the chemical potentials of Pb, Ti and O in four growth conditions illustrated in figure 2. The formation energies of Mn_{Ti}^{2+} still become lower than those of Mn_{Pb} in this case.

In another case (as described in model #2), V_{Pb} is considered in the study of Mn doped PT. When a Mn ion enters the A site, it could compensate V_{Pb}, while if it enters the B site, the V_{Pb} will be left. The formation energies for Mn in different configurations are analyzed as a function of Fermi energy, and are shown in figure 5. Comparing the formation energies of model #1 (not containing V_{Pb}) in figure 4, it can be found that those of Mn_{Ti} have an increase corresponding to the same growth conditions which results in the formation energies of Mn_{Pb} that are obviously lower than those of Mn_{Ti} in figures 5 (c) and 5 (d), while they get close to each other in figures 5 (a) and 5 (b).

The defect formation energies were calculated at corresponding Fermi levels for Mn in different configurations, and listed in table 4 with Fermi levels and the values in [32] too. Their positions are marked with red solid circles for Mn_{Pb} and with black solid squares for Mn_{Ti}, respectively, in figures 4

Table 4. Formation energies E (eV) of different defects at corresponding Fermi levels ε_F (eV) which have been calibrated with the top of the valence band for Mn in different configurations. E_f^A, E_f^B, E_f^C and E_f^D represent defect formation energies in A, B, C and D, four different growth conditions in figure 2, E_f^1, E_f^2 and E_f^3 represent those in three different growth conditions in [32].

Defect	ε_F	E_f^A	E_f^B	E_f^C	E_f^D	E_f^1	E_f^2	E_f^3
Mn_{Pb}^{2+}	1.704	3.850	3.470	5.900	5.900	~2.3	~4.6	~4.6
Mn_{Pb}^{3+}	1.095	3.485	3.105	5.535	5.535	–	–	–
Mn_{Ti}^{2+}	2.298	0.594	0.424	5.294	4.714	–	–	–
Mn_{Ti}^{3+}	1.996	0.874	0.704	5.574	4.994	–	–	–
Mn_{Ti}^{4+}	1.594	1.020	0.850	5.720	5.140	~0.5	~ −1.3	~0.1
Mn_{Ti}^{2+} with V_{Pb}	1.472	4.336	3.786	11.086	10.506	–	–	–
Mn_{Ti}^{3+} with V_{Pb}	1.206	5.024	4.474	11.774	11.194	–	–	–
Mn_{Ti}^{4+} with V_{Pb}	1.009	5.250	4.700	12.00	11.420	–	–	–

and 5, except that for Mn_{Ti}^{3+} due to too short line segment in figure 5, which agree with the line segment of their charge state in the diagrams. Since the defect formation energies have a close relationship with the chemical potential selecting, the values in this paper are slightly different from those in the [32]. The stable charge state is the one which has the lowest formation energy for a given Fermi level [29]. The neutral charge states have obviously higher energies than other charge states, and the formation energies of Mn_{Ti}^{2+} are the lowest in model #1 (not containing V_{Pb}), while those of Mn_{Pb}^{3+} are the lowest in model #2 (containing V_{Pb}). Thus, considering minimization of the defect formation energy, it could be concluded that (1) the neutral Mn defects are more unstable than those of other charge states [33]; (2) Mn ions prefer the B sites in +2 valence state in PT without V_{Pb}, while Mn ions prefer A sites in +3 valence state in PT with V_{Pb}, which shows that A sites are more favored by Mn ions when Pb is deficient.

Considering the change of defect configurations in PT with the concentration of Mn doping, based on the conclusion from model #2 (containing V_{Pb}), a few Pb deficiencies caused by Pb volatilization in PT could be relieved due to the compensation of Mn ions entering the Pb sites in +3 valence state, which results in a decrease of the trapping electronic charge and makes the domain wall motion easier, thus improving ferroelectric and piezoelectric properties of PT [14, 16]. Then, at a further increase of Mn doping concentration, there will be no V_{Pb}'s needing Mn ions to fill, based on the conclusion from model #1 without V_{Pb}, more Mn ions in +2 valence state are more likely to replace Ti^{4+} to increase oxygen vacancy concentration in PT which results in a decrease of the relative permittivity and loss tangent usually [14–18]. The measurement of Electron Spin Resonance also shows that Mn ions coexist mainly in the way of Mn^{2+} and Mn^{3+} in PZT ceramics [14].

3.2.2. Structure

The volumes of 3×3×3 PT supercells with different defects are listed with their change rate compared to that of pure PT in table 5. The supercell has a larger volume change for Mn doping at A site than that for Mn doping at B site at the same valence state, which was also observed in the experimental result of 0.5% Mn doped PZT [16]. Additionally, it becomes larger and larger with Mn ion's valence. The ionic radii of Pb^{2+} and Ti^{4+} are 1.32 Å, 0.64 Å, while those of Mn^{2+}, Mn^{3+} and Mn^{4+} are 0.91 Å, 0.65 Å and 0.53 Å, respectively [34]. Consequently, Mn substituting for Pb could produce a large lattice distortion while its

Table 5. Calculated volumes of PT $3 \times 3 \times 3$ supercells with different defects and their corresponding change rates compared to that of perfect PT.

Configuration	Volume (Å)	Change rate
PT	1689.41	–
PT with Mn_{Pb}^{2+}	1676.33	−0.77%
PT with Mn_{Pb}^{3+}	1668.77	−1.22%
PT with Mn_{Ti}^{2+}	1694.70	0.31%
PT with Mn_{Ti}^{3+}	1684.88	−0.27%
PT with Mn_{Ti}^{4+}	1676.41	−0.77%
PT with Mn_{Ti}^{2+} and V_{Pb}	1688.36	−0.06%
PT with Mn_{Ti}^{3+} and V_{Pb}	1680.00	−0.56%
PT with Mn_{Ti}^{4+} and V_{Pb}	1671.67	−1.05%

Table 6. Average Bader charges (e) of Pb, Ti and O of PT for different Mn doping, respectively, and their changes Δq compared with those of undoped PT, are given in parentheses.

Atoms	undoping	Mn_{Pb}^{2+} (Δq)	Mn_{Pb}^{3+} (Δq)	Mn_{Ti}^{2+} (Δq)	Mn_{Ti}^{3+} (Δq)
Pb	1.35644	1.340324 (−0.016116)	1.34888 (−0.00756)	1.334463 (−0.021977)	1.341407 (−0.015033)
Ti	1.846502	1.856993 (0.010491)	1.859499 (0.012997)	1.840132 (−0.00637)	1.848042 (0.00154)
O	−1.067647	−1.06498 (0.002667)	−1.057343 (0.010304)	−1.078887 (−0.01124)	−1.072041 (−0.004394)

substitution for Ti^{4+} causes a small lattice distortion due to a similar ionic radius between Mn and Ti ions. Greater lattice deformation would lead to the structural change or unstable state of PT eventually by more Mn entering the A site which is not actually found in the experiment. Therefore, it is inferred that Mn ion may enter the A site only at a low concentration while it mainly enters the B site at a high concentration.

3.2.3. Bader charge

Average Bader charges of Pb, Ti and O of PT with and without Mn doping at different sites are listed in table 6, respectively. One Ti ion and one Pb ion correspond to three O ions according to stoichiometric ratio in PT and the increase of positive charge of Ti and Pb ions always corresponds to the increase of negative charge of O ions which could be verified by average Bader charges of Pb, Ti and O ($1.35644 + 1.846502 \approx 3 \times 1.067647$). The charge number of O ion is reduced for Mn entering the A-site compared with undoped PT which indicates that the electronegativity of O becomes weaker. The electronegativity of O could affect the binding force between ions. Thus, when Mn enters the A site, the

Table 7. The Bader charges (e) of Mn ions in different valence states at A and B sites of PT. N_1, N_2 and ΔN represent the electronic numbers of Mn atom, the Bader charges of Mn ions and $N_2 - N_1$.

Defect	N_1	N_2	ΔN
Mn_{Pb}^{2+}	7.00	5.723836	1.276164
Mn_{Pb}^{3+}	7.00	5.632596	1.367404
Mn_{Ti}^{2+}	7.00	5.484108	1.515892
Mn_{Ti}^{3+}	7.00	5.431728	1.568272
Mn_{Ti}^{4+}	7.00	5.374644	1.625356

binding force between ions becomes weaker, which makes the domain movement easier in PT to improve the electromechanical performance of PT, while Mn entering the B site is the opposite.

The bonding mode of Mn ion entering the different position of PT directly affects the charge distribution of PT which results in the change of its performance. The Bader charges of Mn ions at different lattice sites are listed in table 7, respectively. Mn ions lost more electrons entering the B site than entering the A site, which shows that the ionicity of the chemical bond is stronger when Mn ion enters the B site. In addition, the ionicity of Mn increases with its valence.

4. Conclusion

Mn defects in PT have been studied by the first-principles based on the native vacancy defects. The defects of Mn_{Pb} and Mn_{Ti} were analyzed in two different lattice models with and without V_{Pb}s which are the most probable vacancy defects to occur during the growth process of PT. It is found that whether Mn ion enters A or B site of PT is related to its doping concentration. PT prefers to incorporate Mn on Pb sites rather than Ti sites with the Pb deficiencies at a low Mn concentration, while a B-site Mn doping is preferable at a high concentration. Mn ion entering the A site with +3 valence could result in the lattice distortion of PT becoming larger and the electronegativity of O becoming weaker, which makes the domain movement easier in PT to improve the performance of PT.

Acknowledgements

The work was supported by the National Natural Science Foundation of China (No. 11705136), the Special Foundation of Shaanxi Educational Commission (No. 17JK0435), the Natural Science Foundations of Shaanxi Province of China (No. 2018JQ1048 and No. 2020JQ-656).

References

1. Niu X. S., Jia W., Qian S., Zhu J., Zhang J., Hou X. J., Mu J. L., Geng W. P., Cho J. D., He J., Chou X. J., ACS Sustainable Chem. Eng., 2019, **7**, 979–985, doi:10.1021/acssuschemeng.8b04627.
2. Engholm M., Bouzari H., Christiansen T. L., Beers C., Bagge J. P., Moesner L. N., Diederichsen S. E., Stuart M. B., Jensen J. A., Thomsen E. V., Sens. Actuators, A, 2018, **273**, 121–133, doi:10.1016/j.sna.2018.02.031.
3. Kudela P., Radzienski M., Ostachowicz W., Yang Z. B., Mech. Syst. Sig. Process., 2018, **108**, 21–32, doi:10.1016/j.ymssp.2018.02.008.
4. Wang H., Chen Z. F., Xie H. K., Sens. Actuators, A, 2020, **3091**, 112018, doi:10.1016/j.sna.2020.112018.
5. Li J. F., Zhu Z. X., Lai F. P., J. Phys. Chem. C, 2010, **114**, 17796–17801, doi:10.1021/jp106384e.

6. Wongdamnern N., Triamnak N., Ngamjarurojana A., Laosiritaworn Y., Ananta S., Yimnirun R., Ceram. Int., 2008, **34**, 731–734, doi:10.1016/j.ceramint.2007.09.048.
7. Tong S., Ma B. H., Narayanan M., Liu S., Koritala R., Balachandran U., Shi D., ACS Appl. Mater. Interfaces, 2013, **5**, 1474–1480, doi:10.1021/am302985u.
8. Hu G. L., Ma C. R., Wei W., Sun Z. X., Lu L., Mi S. B., Liu M., Ma B. H., Judy W., Jia C. L., Appl. Phys. Lett., 2016, **109**, 193904, doi:10.1063/1.4967223.
9. Mahato D. K., Molak A., Szeremeta A. Z., Mater. Today: Proc., 2017, **4**, 5488–5496, doi:10.1016/j.matpr.2017.06.004.
10. Wang Z., Ren W., Ren J. B., Wu X., Shi P., Chen X., Yao X., Ferroelectrics, 2009, **383**, 151–158, doi:10.1080/00150190902889333.
11. Kozielski L., Adamczyk M., Erhart J., Pawełczyk M., J. Electroceram., 2012, **29**, 133–138, doi:10.1007/s10832-012-9746-z.
12. Zhang M. F., Wang Y., Wang K. F., Zhu J. S., Liu J. M., J. Appl. Phys., 2009, **105**, 061639, doi:10.1063/1.3055338.
13. Feigl L., Pippel E., Pintilie L., Alexe M., Hesse D., J. Appl. Phys., 2009, **105**, 126103, doi:10.1063/1.3141733.
14. He L. X., Li C. E., J. Mater. Sci., 2000, **35**, 2477–2480, doi:10.1023/A:1004717702149.
15. Liu Y. B., Xu Z., Li Z. R., Zhuang Y. Y., Tian Y., Hu D., Song K. X., Guo H. S., J. Alloys Compd., 2018, **742**, 958–965, doi:10.1016/j.jallcom.2018.01.027.
16. Xin H., Ren W., Wu X. Q., Shi P., J. Appl. Phys., 2013, **114**, 027017, doi:10.1063/1.4812226.
17. Hennings D., Pomolun H., J. Am. Ceram. Soc., 1974, **57**, 527–532, doi:10.1111/j.1151-2916.1974.tb10802.x.
18. Yu Y., Wu J. G., Zhao T. L., Dong S. X., Gu H. S., Hu Y. M., J. Alloys Compd., 2014, **615**, 676–682, doi:10.1016/j.jallcom.2014.06.144.
19. Limpijumnong S., Rujirawat S., Boonchun A., Smith M. F., Cherdhirunkorn B., Appl. Phys. Lett., 2007, **90**, 103113, doi:10.1063/1.2711200.
20. Wang L., Yu J., Wang Y., Gao J., J. Mater. Sci.: Mater. Electron., 2008, **19**, 1191–1196, doi:10.1007/s10854-007-9524-x.
21. Dimos D., Schwartz R. W., Lockwood S. J., J. Am. Ceram. Soc., 1994, **77**, 3000–3005, doi:10.1111/j.1151-2916.1994.tb04536.x.
22. Wang J. L., Tang G., Wu X. S., Pu L., J. Mater. Sci., 2014, **49**, 4715–4721, doi:10.1007/s10853-014-8171-x.
23. Kresse G., Joubert D., Phys. Rev. B, 1999, **59**, 1758, doi:10.1103/PhysRevB.59.1758.
24. Kresse G., Furthmüller J., Phys. Rev. B, 1996, **54**, 11169, doi:10.1103/PhysRevB.54.11169.
25. Perdew J. P., Burke K., Ernzerhof M., Phys. Rev. Lett., 1996, **78**, 1396, doi:10.1103/PhysRevLett.78.1396.
26. Robertson J., Warren W. L., Tuttle B. A., J. Appl. Phys., 1995, **77**, 3975–3980, doi:10.1063/1.358580.
27. Xiao P., Fan X. L., Liu L. M., Lau W. M., Phys. Chem. Chem. Phys., 2014, **16**, 24466–24472, doi:10.1039/c4cp03453h.
28. Fang Y. Z., Kong X. J., Wang D. T., Cui S. X., Liu J. H., Chin. J. Phys., 2018, **56**, 1370–1377, doi:10.1016/j.cjph.2018.04.011.
29. Van de Walle C. G., Neugebauer J., J. Appl. Phys., 2004, **95**, 3851–3879, doi:10.1063/1.1682673.
30. Kubota T., Nakamura A., Toyoura K., Matsunaga K., Acta Biomater., 2014, **10**, 3716–3722, doi:10.1016/j.actbio.2014.05.007.
31. Buckeridge J., Scanlon D. O., Walsh A., Catlow C. R. A., Comput. Phys. Commun., 2014, **185**, 330–338, doi:10.1016/j.cpc.2013.08.026.
32. Boonchun A., Smith M. F., Cherdhirunkorn B., Limpijumnong S., J. Appl. Phys., 2007, **101**, 043521, doi:10.1063/1.2654120.
33. Hayashi K., Ando A., Hamaji Y., Sakabe Y., Jpn. J. Appl. Phys. Part 1, 1998, **37**, 5237, doi:10.1143/JJAP.37.5237.
34. Shannon R. D., Acta Crystallogr., Sect. A: Found. Crystallogr., 1976, **A32**, 751–767, doi:10.1107/S0567739476001551.

Центри легування і валентність іонів Mn у $PbTiO_3$ на основі природних дефектів вакансій

Г. Сін, К. Панг, Д.Л. Гао, Л. Лі, П. Жанг

Науковий коледж університету архітектури і технологій м. Ксян, Ксян, 710055, КНР

На основі першопринципного моделювання вивчалися місце легування і валентність іонів Mn у сполуках $PbTiO_3$ (PT) з природними дефектами вакансій. Спершу були вивчені природні дефекти вакансій Pb, O та Ti у PT, і було виявлено, що вакансія Pb є найкращою. При рості PT, легованої Mn, переважним має бути заміщення іонами Mn з валентністю +3 іонів Pb в A-центрах, коли концентрація Pb є недостатньою в умовах рівноваги. Це обумовлено виключно мінімізацією енергії утворення і може призвести до більшої дисторсії гратки PT. Крім того, коли Mn потрапляє на місце Pb, електронегативність O стає слабшою, що полегшує рух доменів в PT і покращує характеристики цієї сполуки, тоді як заміщення іонами Mn іонів Ti в B-центрі має протилежний ефект.

Ключові слова: *легування Mn, сполуки PT, природні дефекти, енергія утворення дефектів, заряд Бейдера*